Energy materials



Effect of proton irradiation on anatase TiO₂ nanotube anodes for lithium-ion batteries

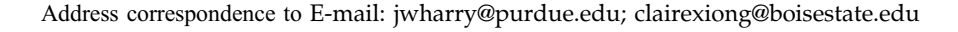
Kassiopeia A. Smith¹, Andreas I. Savva¹, Keyou S. Mao², Yongqiang Wang³, Dmitri A. Tenne⁴, Di Chen³, Yuzi Liu⁵, Pete Barnes¹, Changjian Deng¹, Darryl P. Butt⁶, Janelle P. Wharry^{7,*}, and Hui Xiong^{1,*}

Received: 22 March 2019 Accepted: 3 July 2019 Published online: 11 July 2019

© Springer Science+Business Media, LLC, part of Springer Nature 2019

ABSTRACT

The role of defects in the charge transfer and transport properties of electrode materials for lithium-ion batteries has recently garnered increased interest. It is widely recognized that ion irradiation promotes the formation of defects within a crystalline solid. Among all ion species used for irradiation, protons are expected to create primarily simple Frenkel pair point defects without significantly changing the stoichiometry of the damaged region of the target material. This work investigates the effect of proton irradiation at varying temperatures on the electrochemical properties of anatase TiO₂ nanotube (TiO₂-NT) electrode for lithium-ion battery applications. Anatase TiO₂-NTs are irradiated at both room temperature (25 °C) and 250 °C and compared with non-irradiated control specimens. Characterization by Raman spectroscopy and XRD suggests that the irradiation at both temperatures does not alter the long-range order of the nanotubes. However, high-resolution TEM reveals that defect clusters are formed upon irradiation and increase in size with increasing temperature. Both irradiated samples exhibit increased capacity and enhanced rate capability compared with the non-irradiated control, which can be explained by increased storage sites as well as improved Li⁺ diffusivity due to the presence of irradiation-induced defects. This study presents a unique perspective on pathways to engineer functional nanostructured electrode materials by tailoring irradiation conditions.





¹ Micron School of Materials Science and Engineering, Boise State University, 1910 University Drive, Boise, ID 83725, USA

² School of Materials Engineering, Purdue University, 701 West Stadium Avenue, West Lafayette, IN 47907, USA

³Ion Beam Materials Laboratory, Los Alamos National Laboratory, Los Alamos, NM, USA

⁴Department of Physics, Boise State University, 1910 University Drive, Boise, ID 83725, USA

⁵Center for Nanoscale Materials, Argonne National Laboratory, Lemont, IL, USA

⁶College of Mines and Earth Sciences, University of Utah, 115 S 1460 E, Salt Lake City, UT 84112, USA

⁷School of Nuclear Engineering, Purdue University, 400 Central Drive, West Lafayette, IN 47907, USA

Introduction

Rechargeable lithium-ion batteries (LIBs) were revolutionary in the development of portable electronics and are considered the most promising energy storage devices for a range of next-generation technologies [1]. Titanium dioxide (TiO₂) anodes have gained attention over the years due to their inherent safety, stability, and cost [2-4]. In addition, TiO₂ has a theoretical capacity of 335 mAh g^{-1} (or 1.0 Li per TiO₂), which is comparable to commercial graphite electrodes (372 mAh g⁻¹) [4]. Among all polymorphs of TiO₂, anatase has been widely studied as an anode for LIBs. Anatase has a tetragonal body-centered structure with the space group $I4_1/amd$ and is made of edge-sharing TiO₆ octahedra [5]. The structure can be visualized as stacking 1D zigzag chains of edgesharing octahedra, resulting in zigzag channels within the framework allowing for facile diffusion of lithium ions [2].

Original attempts to use anatase as an anode focused on microcrystalline structures; however, these exhibit only moderate specific capacity, with a maximum uptake of 0.5 Li per TiO₂ due to limited room-temperature conductivity [6]. This limitation spurred the development of nanoscale TiO₂ electrodes, leading to significant improvement in reported electrochemical behavior [1, 7–16]. Using nanoscale electrodes allows for increased contact area between the electrode and electrolyte and reduced Li⁺ transport distances, which facilitate high-power applications [7, 10, 14–18]. The reaction of Li⁺ with TiO₂ can be expressed as:

$$xLi^{+} + TiO_{2} + xe^{-} \leftrightarrow Li_{x}TiO_{2}$$
 (1)

Interstitials and vacancies present in the structure play an important role in the atomic rearrangement and allow for improved storage capacity [19, 20]. Recent works have suggested that the introduction of intentional structural defects may enhance the electrochemical charge storage properties of transition metal oxide electrodes [19, 21–24]. One such method is to use ion irradiation to generate defects within the target material [19].

Ion irradiation is known to generate a wide variety of defects in ceramics—including point defect generation, formation of defect clusters, amorphization by accumulation of point defects and defect clusters, or direct impact amorphization—as has been

reviewed in several reports [25–27]. The nature and extent of the irradiation-induced defects are dependent upon numerous parameters, including anion/cation species and their displacement and migration energies [28–30], irradiating beam current (i.e., beam heating) [31], structural rigidity and constraints [29], bond hybridization [32], irradiation-induced bond evolution (e.g., bond breaking/reforming, dangling bonds, kinks) at amorphous-crystalline interfaces [33–35], and the energy loss mechanism of the irradiating particles.

The energy loss mechanism is believed to be among the most critical parameters influencing the irradiated microstructure evolution. In general, for low irradiating particle energies, energy loss tends to occur through nuclear stopping, which can be described by the binary collision approximation (BCA). Nuclear stopping produces defects through the damage cascade process, and in ionic solids, these cascades manifest as disordered or amorphous regions in the microstructure. Electronic stopping is the dominant energy loss mechanism for irradiating particles with high energies. Electronic stopping is commonly understood through the inelastic thermal spike model [36-38], in which dense electronic excitations transfer energy to the material and generate localized heating, resulting in visible ion "tracks" which are highly disordered to amorphous regions surrounding the ion path. An alternative theory of ionization-induced diffusion [39] has also been proposed, in which defect growth is enhanced by accelerated diffusion when ionization (i.e., electronic) energy losses are dominant. At intermediate ion energies (several hundred keV to several MeV), there is evidence for synergistic nuclear and electronic energy losses in ceramic materials, producing a higher local defect density (i.e., greater local disordering) than would result from sequential evolution of damage cascade and thermal spike processes [40-46].

In recent years, several studies have brought attention to the effect of irradiation on TiO₂. Density functional theory simulations on this topic have suggested that rutile has greater resistance to amorphization than anatase TiO₂ polymorphs due to atomic packing densities [47–49]. This supposition was supported by Uberuagua [50], Qin [51], and Lumpkin [48], who further elucidated the mechanisms of defect accumulation and amorphization resistance. Li et al. [52] studied the effect of



irradiation temperature and found that higher temperatures allow for point defect mobility, leading to enhanced damage recovery, whereas room-temperature irradiation produces point defects that remain in the crystalline lattice. Hartmann et al. [53] later suggested that using lighter irradiation species, such as He⁺, is more likely to amorphize target substrates than heavy noble gases such as Xe²⁺ and Ne⁺. Schmuki et al. [54] recently studied the effect of proton irradiation on anatase TiO2 films for photocatalytic evolution and showed that proton implantation induced specific defects which created cocatalytic centers and enhanced photocatalytic activity. Finally, in our previous study, it was shown that when irradiated with 200 keV protons at 250 °C, amorphous TiO₂ nanotubes (TiO₂-NTs) undergo a phase transformation to a disordered rutile phase leading to an increase in capacity and rate capabilities [19].

Herein, we report the study on the effect of proton irradiation on anatase TiO2-NT electrodes. Implantations were carried out using 195 keV protons to an average dose of 0.25 displacements per atom (dpa) at temperatures of 25 °C and 250 °C. Structural characterization by Raman spectroscopy and X-ray diffraction (XRD) suggests that no major change in the longrange order of the crystalline sample occurs under irradiation. Furthermore, crystallinity is confirmed by selected area electron diffraction (SAED) and highresolution transmission electron microscopy (HRTEM). However, darkly contrasting defects are visible by HRTEM and appear to have a disordered structure in both the RT and HT irradiated specimens. These defects increase in size with irradiation temperature. Electrochemical impedance troscopy (EIS) was conducted, and it was found that both irradiated samples exhibit reduced charge transfer resistance and increased lithium diffusivity. Both the samples irradiated at 250 °C and 25 °C demonstrate improved capacity at low rate and superior rate capability compared to the non-irradiated anatase TiO₂-NT. These findings underscore the role of the irradiation-induced defects in promoting electrochemical performance.

Materials and methods

Materials

TiO₂-NTs were synthesized by electrochemical anodization, the method for which has been published previously [24, 55, 56]. To summarize, pure titanium foil (0.127 mm, 99.8%, Alfa Aesar) was electropolished [57], followed by a three-step sonication in acetone, isopropyl alcohol, and deionized (DI) water. The back of the Ti foil was protected by packaging tape to ensure uniform current distribution. The anodization was carried out in a two-electrode cell with Pt mesh as the counter electrode. The anodization was conducted for 10 min under a constant voltage of 15 V in an electrolyte of 0.36 M ammonium fluoride (Aldrich) in 95 vol% formamide (Fisher) and 5 vol% DI water. The anodized samples were then ultrasonically cleaned in DI water for 30 s. Anodization creates TiO2-NTs inherently connected to the Ti substrate, which acts as both the current collector and a rigid backing for handling and characterization. This method of material synthesis eliminates the need for conductive carbon additives and polymer binders typically used in electrodes for LIBs. Anatase TiO₂ was made by annealing the as-prepared TiO₂ NTs in a mixture of ultra-pure 20% O₂/ balance Ar gas at 450 °C for 4 h.

Irradiation

The TiO₂-NT films were irradiated with 195 keV protons in a 200 kV Danfysik ion implanter at Los Alamos National Laboratory. The accelerator beam line was maintained at 4×10^{-7} torr throughout the experiment. Specimens were mounted onto a copper irradiation stage which contains embedded heating elements and thermocouples for varying and measuring sample temperature during the ion irradiation/implantation. The ion fluence was accurately measured by a standard four-corner Faraday cup assembly. During irradiation, the focused proton beam was raster-scanned across samples, yielding a dose rate of 9.6×10^{-6} dpa s⁻¹.

The irradiation damage profile was calculated using the Stopping and Range of Ions in Matter (SRIM-2013) program using the "Quick K-P Calculation" mode. Because the software cannot depict single-walled nanotube structures, a layer of TiO₂ (density of 4.23 g cm⁻³) having a thickness



equivalent to the length of the nanotubes was modeled as a conservative approach. Displacement energy for titanium and oxygen was set to 25 and 28 eV, respectively. The 195 keV proton beam produces a relatively uniform damage profile through 1.1 μm region (Fig. 1). The damage production rate at the flat region was $\sim 1.7 \times 10^{-3}$ vacancies per ion-Å at the TiO₂ matrix. Nanotube anodization parameters were tailored such that the irradiation damage would be uniform throughout the nanotube length by ensuring that the tube length would be less than the calculated depth of the damage peak. This leads to an average of 0.25 dpa along the length of the TiO₂-NT when the ion fluence of 2.18×10^{17} ions cm⁻² was used in the experiment. However, Schmuki et al. [54] suggested that the actual damage depth in a TiO2-NT film may be greater due to the porosity, potentially resulting in a lower average dpa.

Electrochemical testing

Li half-cells were assembled in coin-type cells (Hohsen 2032) with Li metal foil as the negative electrode, a 2325-type polymer separator, and 1.2 M LiPF₆ in ethylene carbonate/ethyl methyl carbonate (3:7 weight ratio) electrolyte (Tomiyama). Half-cells were cycled galvanostatically at varying currents between 2.5 and 0.9 V versus Li/Li⁺ using an automated Maccor battery tester at ambient temperatures. Electropolishing the Ti metal before anodization allows for formation of uniform, well-adhered nanotubes. The downside of the high adhesion is the increased chance of error when stripping the active oxide from

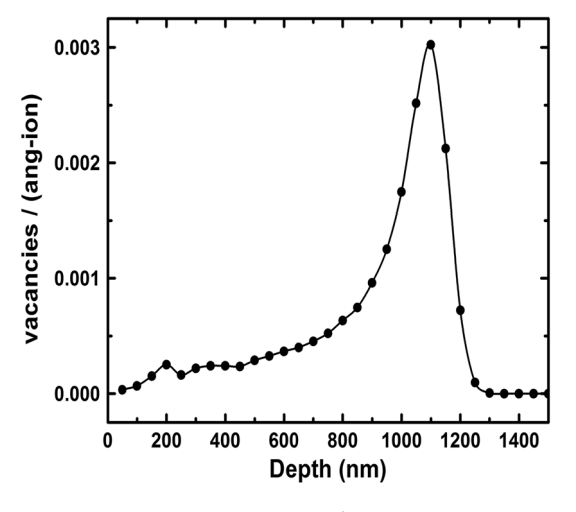


Figure 1 Damage depth profile of H^+ ions on anatase TiO_2 by SRIM calculation.



the Ti metal substrate to calculate gravimetric capacity. To get around this difficulty, areal capacity was instead used by obtaining accurate measurements of the electrode via microscopy.

Three-electrode cells for electrochemical impedance spectroscopy (EIS) were made using ECC-Ref cells (EL-Cell) with lithium metal as both counter and reference electrodes. Mott–Schottky measurements were carried out in three-electrode cells using a Bio-Logic Science Instruments potentiostat/galvanostat. EIS was conducted at a frequency range from 100 kHz to 5 MHz at open circuit voltage by applying a sinusoidal voltage with an amplitude of 5 mV.

Electron microscopy

Scanning electron microscopy (SEM) images were recorded with a FEI Teneo field emission microscope operating at 5 kV. SEM imaging was conducted while the NTs remained affixed to the Ti substrate. Transmission electron microscopy (TEM) images, including HRTEM and SAED, were recorded with a FEI (now Thermo Fisher Scientific) Tecnai TF30-FEG S-Twin Scanning TEM (STEM) operating at 300 kV at the Microscopy and Characterization Suite (MaCS) in the Center for Advanced Energy Studies (CAES) as well as a JEOL 2100F with the accelerating voltage of 200 kV at the Center for Nanoscale Materials in Argonne National Laboratory. TEM specimens were prepared by scraping irradiated NTs from their Ti substrate, then suspending the NTs on a carbon TEM grid.

Raman spectroscopy and X-ray diffraction

Raman spectra were measured using UV excitation, 325 nm lines of a He–Cd laser. The UV Raman spectra were measured in backscattering geometry using a Jobin–Yvon T64000 triple spectrometer equipped with a liquid nitrogen-cooled multichannel CCD. The 325 nm line of He–Cd laser was used for excitation; maximum laser power density was 0.5 W mm⁻² at the sample surface. Spectra were recorded at 10 K using an evacuated closed-cycle helium cryostat.

X-ray diffraction (XRD) was obtained by Rigaku Miniflex diffractometer with Cu K_{α} irradiation at $\lambda = 1.5406$ Å.

Electrical conductivity measurements

Two-point conductivity measurements were used to determine the out-of-plane conductivity of the nanotubes. Gold wires are connected to the sample surface and the back of the Ti foil using \sim 2-mm-diameter drop of silver paint (Figure S2, Supporting Information). The gold wires on the top of the sample were used to apply a current of $10~\mu A$ while the wires on the back of the sample measure voltage. A Keithley 237 High Voltage Source Measure Kit was used to apply the current to each sample, and a Keithley 2000 Multimeter was used to record the resulting voltage. The applied bias was then reversed to ensure the validity of the measured value.

Results and discussion

Figure 2a shows the SEM top view after anodization and annealing, where the individual tubes are approximately 1 μ m in length with a 60 nm (\pm 5 nm) outer diameter and approximately 10 nm (\pm 5 nm) wall thickness. As reported previously, the structure of the TiO₂-NT is maintained after irradiation (Fig. 2b) [19].

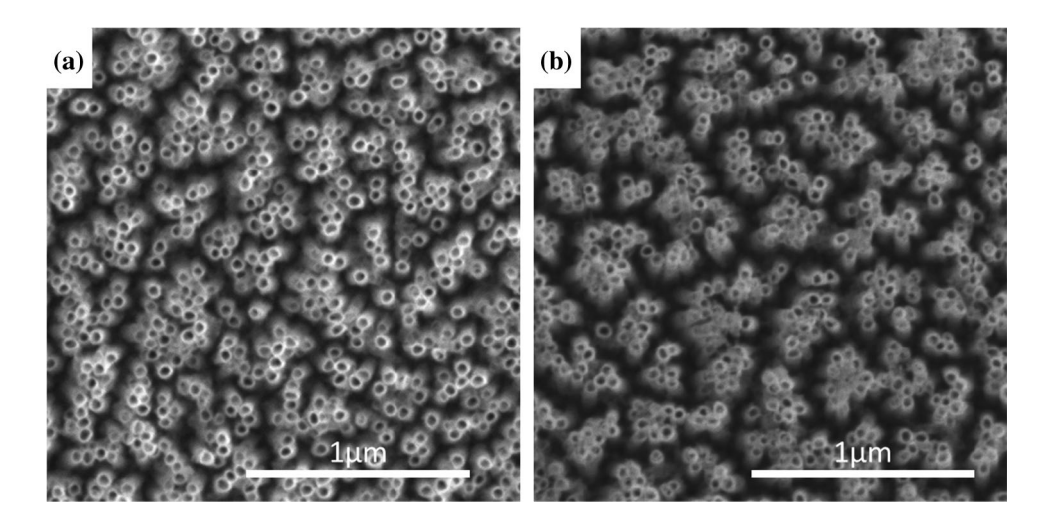
Structural and microstructural characterization

Microstructural characteristics of the TiO₂-NT samples before and after irradiation were analyzed by Raman spectroscopy, XRD, and TEM. Raman spectra measured with 325 nm laser sample the top 5–10 nm of the specimen surface [58]. Anatase TiO₂ has six

characteristic Raman active vibrational modes which are located at 144, 196, 639 cm⁻¹ and are designated as $E_{g(1)}$, $E_{g(2)}$ and $E_{g(3)}$, respectively, two B_{1g} modes at 397 and 519 cm⁻¹, designated as $B_{1g(1)}$, and $B_{1g(2)}$, respectively, and an A_{1g} mode at 513 cm⁻¹ [59–63]. The Raman spectra of both the high-temperature (HT, 250 °C) and room-temperature (RT) irradiated samples compared to the unirradiated control sample are shown in Fig. 3. The spectra were analyzed with Lorentzian fitting. The resulting analysis is shown in Table S1 (Supporting Information). No statistically relevant alteration in the peak positions or full width at half maximum (FWHM) was observed in the HT and unirradiated control samples. (The difference is $< 1 \text{ cm}^{-1}$, i.e., within experimental error.) While the shift in peak positions is minimal, it is worth noting that there is a slight blueshift in the $E_{g(3)}$ mode of the RT sample, which indicates defect formation as it has been found that $E_{g(3)}$ mode is the most sensitive to the presence of defects in anatase TiO₂ nanocrystals [64]. The Scherrer equation [65] was used to analyze the crystallite size from the XRD results (Fig. 4), which indicate that proton irradiation had no significant effect on the size of the crystallites (Table S2, Supporting Information).

The microstructure was also analyzed by TEM, specifically using HRTEM (Fig. 5). Through conventional bright-field TEM, one can observe that the overall NT structure is maintained throughout irradiation (Fig. 5a-c), corroborating SEM results. Crystallinity of the TiO₂-NTs is validated by HRTEM (Fig. 5d–f). Large grains (i.e., > 25 nm diameter) having ordered, anatase structures are observed in the unirradiated specimen, which is consistent with

Figure 2 a As-prepared amorphous ${\rm TiO_2}$ nanotubes, b ${\rm TiO_2}$ nanotubes after annealing and irradiating with protons at 25 °C.





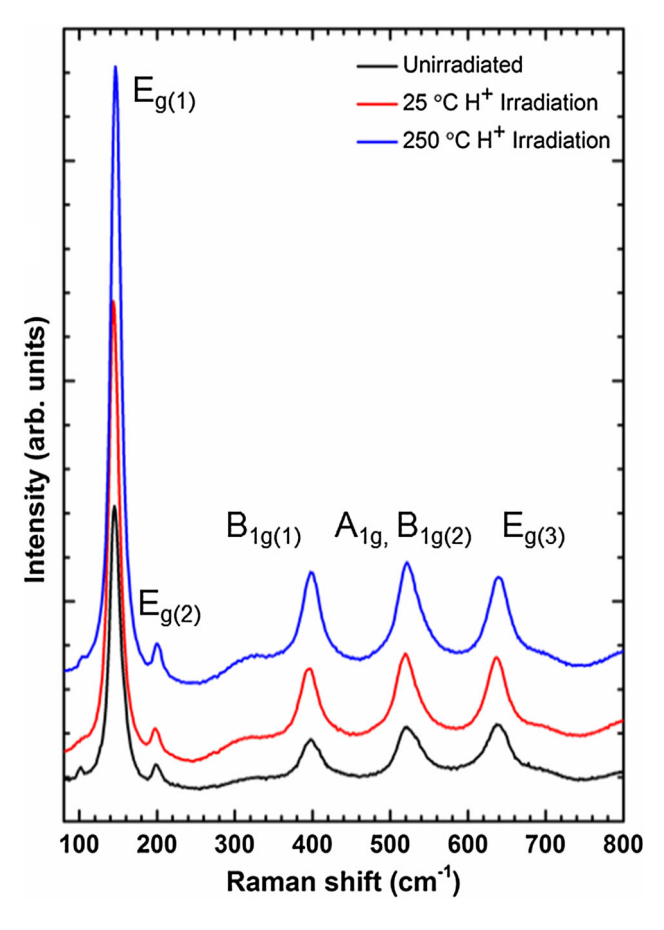


Figure 3 Raman spectra of non-irradiated anatase nanotubes (black); $\mathrm{H^+}$ -irradiated anatase nanotube at 25 °C (red) and $\mathrm{H^+}$ -irradiated anatase nanotube at 250 °C (blue).

previous result [19]. The irradiated specimens also display ordered regions, although the diameter of these regions (~ 5-10 nm) is markedly reduced compared to the unirradiated specimen. Although the observation of ordered regions in all specimens supports the aforementioned XRD observations, there is also TEM evidence of irradiation-induced nanostructuring and/or disordering. Namely, the fast Fourier transforms (FFT) of the HRTEM images show a tendency toward asymmetry with irradiation (Fig. 6a-c), which suggests some loss of crystallinity. At the same time, selected area electron diffraction (SAED) patterns of the irradiated and unirradiated control specimens (Fig. 6d-f) all have a polycrystalline anatase structure, which is consistent with the XRD results. However, the irradiated SAED patterns have a denser distribution of smaller diffraction spots on each ring, corroborating the irradiation-induced grain size reduction observed by HRTEM. Thus, irradiation is believed to introduce some disordering and/or nanostructuring, but overall crystallinity is maintained. Irradiation-induced disordering is consistent with the irradiation-induced amorphization of numerous ceramics including apatite silicates [66], CePO₄ nanoparticles [67], MgAl₂O₄ [68], GaAs [34, 35, 69], Si, Ge, GaP, and InP [34, 35], and LaPO₄, ScPO₄, and zircon (ZrSiO₄) [29] with electron irradiation, and Al₂O₃ and H₂Ti₃O₇ with O or N ion irradiation [70, 71]. Notably, these studies in the archival literature span a wide range of irradiation energy loss

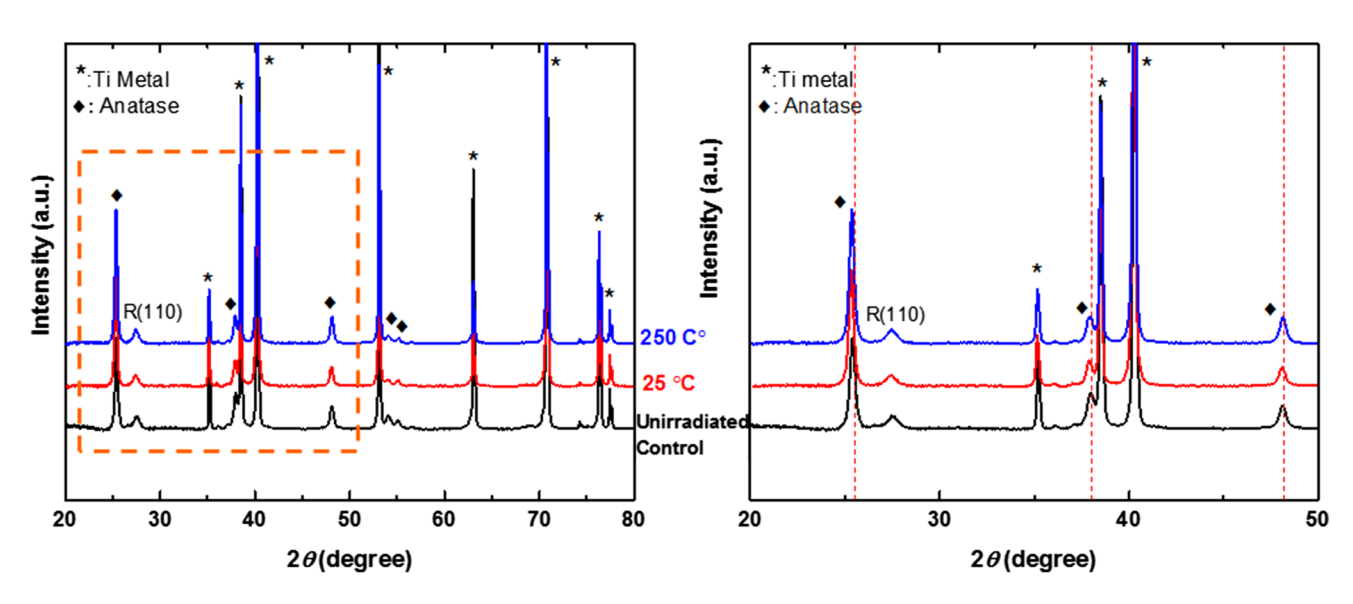


Figure 4 XRD spectra a of TiO₂ nanotube samples before and after proton irradiation and b expanded region in a.



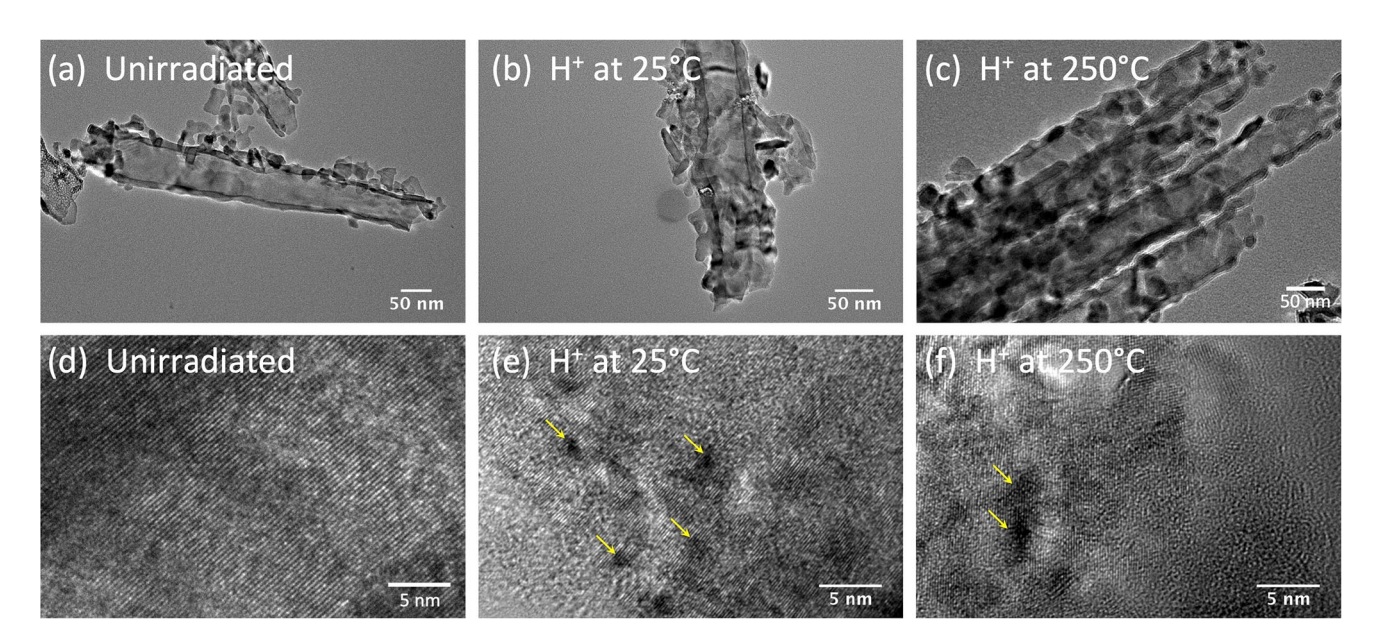


Figure 5 Bright-field TEM of **a** unirradiated anatase nanotube, **b** H⁺-irradiated anatase nanotube at 25 °C, **c** H⁺-irradiated anatase nanotube at 250 °C; and HRTEM of **d** unirradiated anatase

nanotube, e $\mathrm{H^+}$ -irradiated anatase nanotube at 25 °C, f $\mathrm{H^+}$ -irradiated anatase nanotube at 250 °C.

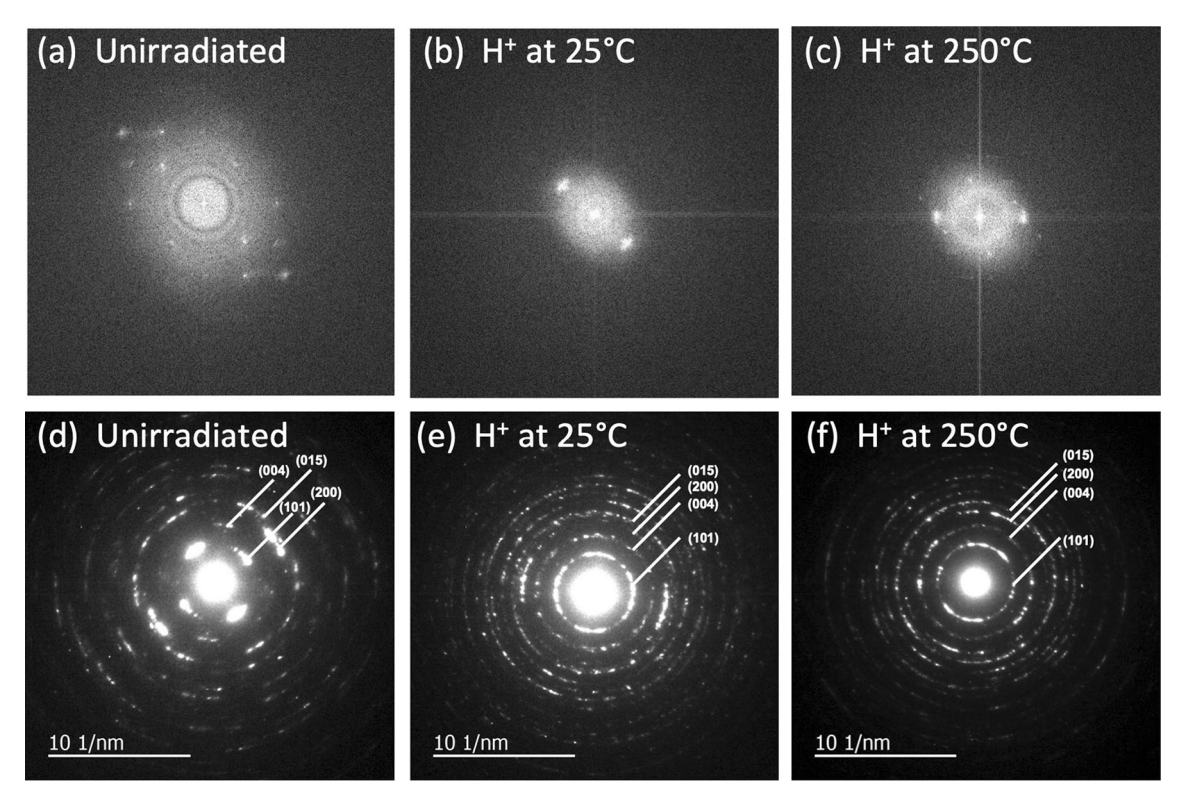


Figure 6 FFT images corresponding to Fig. 5d–f, from **a** unirradiated anatase nanotube, **b** H^+ -irradiated anatase nanotube at 25 °C, **c** H^+ -irradiated anatase nanotube at 250 °C,

and TEM selected area electron diffraction patterns from d unirradiated anatase nanotube, e $\mathrm{H^+}$ -irradiated anatase nanotube at 25 °C, f $\mathrm{H^+}$ -irradiated anatase nanotube at 250 °C.



mechanisms, including both electronic stopping-dominated and nuclear stopping-dominated.

The possible nucleation of irradiation-induced features is also worth noting, specifically the darkly contrasting defects (indicated by arrows in Fig. 5e–f) that appear to have a disordered structure in both the 25 °C and 250 °C irradiated specimens. The average size of these defects increases with irradiation temperature. Features similar in appearance have also been reported in rutile TiO2 irradiated with 1 MeV Kr²⁺ and low-energy Ar⁺ [72, 73]. In those reports, the diffraction maxima are attributed to lattice distortions associated with off-stoichiometry at interfaces between the TiO2 and irradiation-induced amorphous regions. More generally in a variety of ceramics, irradiation has been found to nucleate defect clusters (e.g., dislocation loops) or nanoparticles, both of which have similar TEM diffraction contrast as the defects observed herein [19, 74-78].

Electronic energy losses are dominant for the proton energies used in this study [79, 80]. The observed irradiated microstructure containing nanoscopic regions of disorder is consistent with the theory of inelastic thermal spikes [36–38], which form highly localized regions of disordering. At the same time, the diffraction contrast features—which we postulate could be associated with off-stoichiometry or irradiation defects—may agglomerate due to the proposed theory of ionization-induced diffusion [39]. Hence, we believe there are several plausible mechanistic explanations for the observed microstructures and defects, but the precise nature of these defects cannot conclusively be determined.

Electrochemical characterization

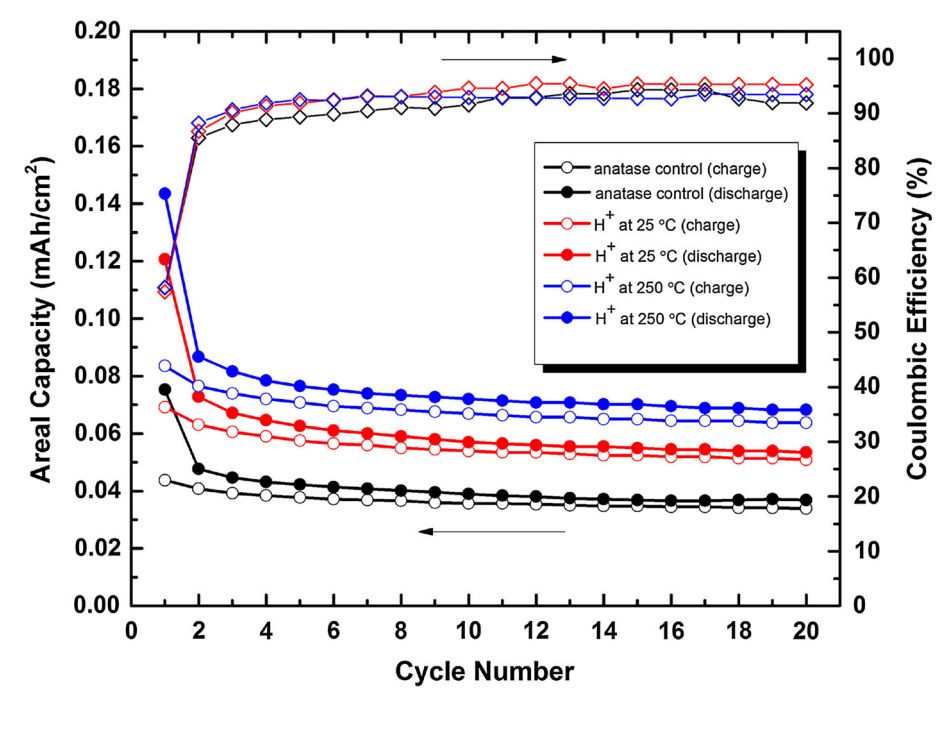
After microstructural characterization, the electrodes were evaluated in Li half-cells. The non-irradiated anatase control sample has an initial charge capacity of 4.37×10^{-2} mAh cm⁻², which leveled off to 3.57×10^{-2} mAh cm⁻² at a C/12 rate (nC: charge/discharge in 1/n hour) after 20 cycles (Fig. 7), which is consistent with literature values of similar material [18]. This capacity is significantly lower than what was observed for the irradiated nanotube electrodes. The RT TiO₂ electrode has an initial charge capacity of 6.92×10^{-2} mAh cm⁻², which stabilized at 5.39×10^{-2} mAh cm⁻² after ten cycles, whereas the HT electrode exhibited a charge capacity of 8.35×10^{-2} mAh cm⁻², which leveled off at

 6.69×10^{-2} mAh cm⁻² by the tenth cycle. This correlates with a 33% and 46% increase in capacity for the RT and HT irradiations, respectively. Additionally, the initial Coulombic efficiency (ICE) of the nonirradiated control, the RT sample, and the HT sample is 58%, 57%, and 58%, respectively. There is no significant effect of the proton irradiation on the samples regarding the ICE compared to the non-irradiated control. The CEs for the electrodes stabilized at the tenth cycle and reached 91% for the non-irradiated control, 94% for the RT sample, and 92% for the HT sample. The proton-irradiated electrodes have slightly higher CEs compared to the control, though these values are within the expected deviation. Further, all samples exhibit good cycling stability at extended cycles (Figure S2, Supporting Information), suggesting that the proton irradiation does not affect TiO₂-NT electrodes adversely in terms of stability.

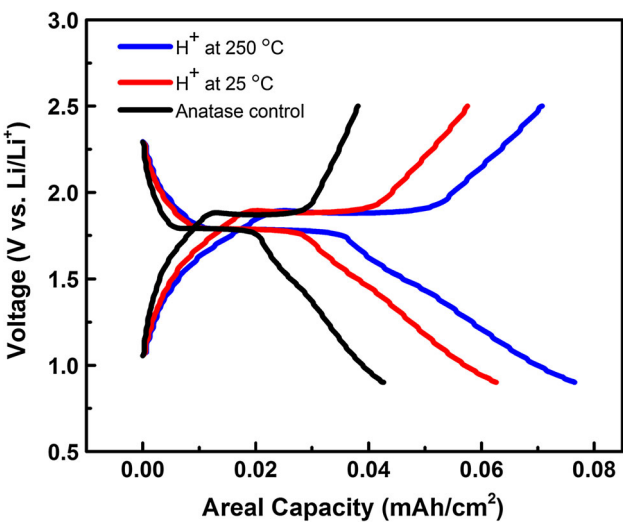
Figure 8 compares the charge/discharge profiles of the irradiated and control anatase samples cycled between 0.9 and 2.5 V (vs. Li/Li⁺) at C/12. Li⁺ ions insert in the anatase TiO2 NT electrodes via a twophase mechanism, which occurs at the characteristic plateau of approximately 1.7 V vs Li/Li⁺, indicating the coexistence of a Li-poor phase Li_{0.05}TiO₂, which maintains the original anatase structure (space group: *I4*₁/amd) and a Li-rich phase Li_{0.5}TiO₂ (space group: Imma) [3]. After irradiation, both the HT and RT samples display this two-phase region. On the other hand, the overall capacity contribution from the sloping regions (calculated by taking the capacity from the sloping regions over the total cell capacity) is 78%, 66%, and 58% for the HT, RT, and non-irradiated control samples, respectively. This trend in capacity contribution suggests that the overall increase in capacity with irradiation is attributed to larger sloping regions, which are associated with increased defect sites where ions insert into a host structure with a distribution of energies [81]. For comparison, the proton-irradiated amorphous samples from our previous work [19] undergo irreversible phase transformation to a mixture of disordered anatase and rutile phase at room temperature and to a primarily disordered rutile phase at 250 °C, both displaying sloping characteristics in the voltage profiles in contrast to the anatase TiO2-NT samples under proton irradiation. The distinct difference in microstructure evolution and corresponding electrochemical properties of amorphous and anatase TiO2-NT under proton irradiation suggest



Figure 7 Areal capacity versus cycle number at low rate (C/12) of non-irradiated anatase nanotube (black), 25 °C H⁺-irradiated nanotube, and 250 °C H⁺-irradiated nanotube electrodes.



350



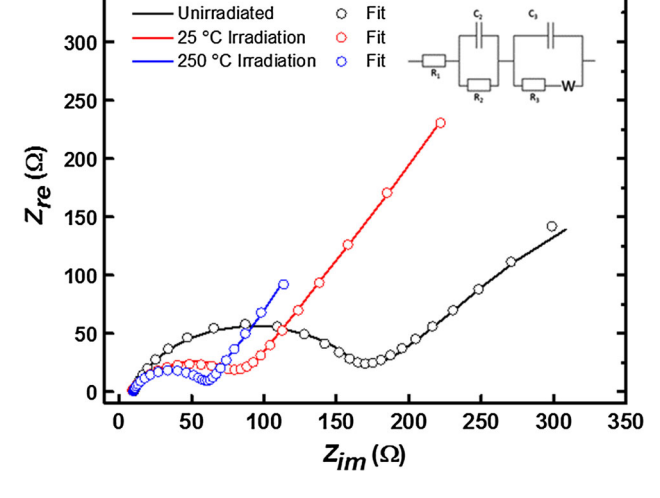


Figure 8 Charge/discharge voltage profiles comparing the fifth cycle of the non-irradiated (black), 25 $^{\circ}$ C H⁺-irradiated nanotube (red), and 250 $^{\circ}$ C H⁺-irradiated nanotube (blue) electrodes.

Figure 9 Nyquist plots of non-irradiated, 25 °C H⁺-irradiated nanotube, and 250 °C H⁺-irradiated nanotube electrodes.

that defect evolution and disordering play a significant role in the charge storage mechanisms in such metal oxide electrodes.

Electrochemical impedance spectroscopy (EIS) is used to better understand the charge storage and transport mechanism behind the variance in electrochemical performance. A modulating potential of small amplitude is applied to the working electrode in a three-electrode cell; the resulting current allows for exploration of charge storage behavior [82].

Nyquist plots for the irradiated and control samples are shown in Fig. 9. These plots contain convoluted semicircles at the high/medium frequency range, followed by a straight line at lower frequencies. The equivalent circuit used to model this system is shown in the inset of Fig. 9. In this equivalent circuit, R_1 is the bulk resistance of the cell (electrolyte, separator, electrode), C_2 and R_2 belong to the capacitance and resistance of the surface process at the TiO₂ electrode surface, C_3 and C_4 correspond to the main semicircle, which represents capacitance and resistance for the



charge transfer process at the electrode, and *W* is the Warburg impedance from the diffusion of Li⁺ ions within the electrode [83–85]. The Nyquist plots show that the charge transfer resistance of HT sample is lower than that of the RT sample, while both irradiated samples have a lower charge transfer resistance than the non-irradiated anatase control, suggesting enhanced charge transfer kinetics in the irradiated samples. Once the data have been fit to an equivalent circuit, Li diffusivity values can be calculated from the Warburg impedance by the equation [86, 87]:

$$D_{\rm Li} = \frac{R^2 T^2}{2C_{\rm Li}^2 \sigma^2 n^4 F^4 A^2} \tag{2}$$

where R is the gas constant, T is the absolute temperature, C_{Li} is the Li concentration in the electrolyte, n is the transferred charge, F is Faraday's constant, and A is the geometric surface area. The electrodes exhibit diffusivities of 2.3×10^{-13} cm² $1.0 \times 10^{-12} \text{ cm}^2 \text{ s}^{-1}$, and $1.3 \times 10^{-11} \text{ cm}^2 \text{ s}^{-1}$ for the non-irradiated control, RT, and HT samples, respectively. Note that the Li⁺ diffusivity of the irradiated samples is 1-2 orders of magnitude higher than that from the non-irradiated control. Furthermore, out-ofplane electrical conductivity measurements were carried out using a two-point measurement [48]. Both RT and HT irradiated TiO₂-NT specimens exhibit an increase in electrical conductivity compared with the control, with the RT TiO₂-NT specimen being the highest (Table S3, Supporting Information). The conductivity of the non-irradiated sample is comparable with previously reported two-point measurements on anatase TiO₂-NT [88, 89]. These results suggest that proton irradiation promotes both electrical and ionic conductivity, which could be explained by the irradiated microstructures observed by HRTEM. We have noted that irradiation enhances disorder and potentially creates defected regions having off-stoichiometric boundaries. It is well known that disorder, interfaces, and off-stoichiometry can enhance both electrical and ionic conductivity, as recently reviewed in Ref. [90]. Because of the ex situ nature of our characterization and electrochemical charge cycling, we are not currently able to determine how these defects interact with Li or evolve during Li insertion.

The rate capability study was carried out to assess how irradiation affects the kinetics of the TiO₂-NT electrodes (Fig. 10). The rate capability of HT TiO₂-NT electrode is the best among the three electrodes,

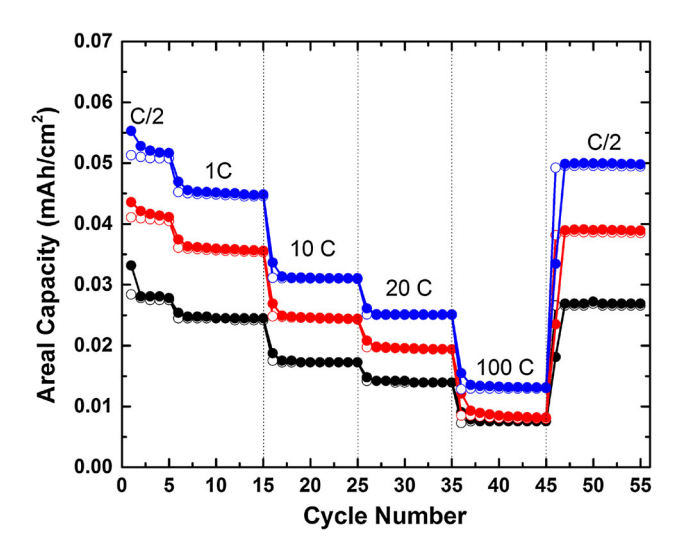


Figure 10 Rate capabilities of non-irradiated (black), 25 °C H⁺-irradiated nanotube (red), and 250 °C H⁺-irradiated nanotube electrodes (blue). Solid circle: discharge capacity, open circle: charge capacity.

and the non-irradiated TiO₂-NT electrode performs the worst. This is especially apparent at the high rates. At a very high rate of 20C, both irradiated electrodes have higher capacity than the non-irradiated TiO₂-NT control electrode, and at 100C rate, the capacity of both RT and non-irradiated TiO₂-NT electrodes drops off drastically while the HT irradiated electrode maintains about 20% of the low-rate capacity. While the increase in electrical conductivity plays an important role in the increase in rate capability, the high-temperature irradiated specimen outperforms the room-temperature irradiated sample, likely because of the high lithium diffusivity and high capacitive behavior [19] (large sloping regions).

It is well known that the evolution of an irradiated microstructure is strongly influenced by the irradiation temperature [91]. Specifically, diffusion is sufficiently limited at irradiation temperatures ≤ 25 °C, so the point defects produced by proton irradiation are relatively immobile and remain in the material as either single-point defects or nm scale defect clusters [91]. This is typically observed as local disordering or amorphization in ceramics [38, 92]. It has been shown in numerous ceramic materials—namely SiC, sapphire, alumina, aluminum nitride, silicon nitride, beryllium oxide, and a carbon fiber composite—that as the irradiation temperature increases $\gtrsim 60$ °C, a higher irradiation dose is necessary to induce disordering or amorphization [93]. Given the wide range of ceramics that follow this trend, a similar behavior



is likely to occur in TiO_2 . This means that the point defects are sufficiently mobile and can form subnanoscale to few-nm-diameter defect clusters, such as those observed in the 250 °C irradiated specimens herein (Fig. 5c, f). If such clusters are comprised of vacancies, they provide sufficient volume for Li intercalation as well as internal surface area. If these clusters formed from interstitials, they provide sufficient strain to the surrounding material matrix that provides free volume for Li intercalation. Hence, it is not unreasonable that the higher temperature irradiation will have enhanced electrochemical performance as compared to the 25 °C irradiation, especially given the TEM and HRTEM results obtained here.

Conclusions

Proton irradiation was carried out on TiO₂-NT at 25 °C and 250 °C to an average flat region damage of ~ 0.25 dpa. Post-irradiation electrochemical testing and microstructural characterization were conducted to evaluate and explain the relative electrochemical performance of the irradiated specimens as compared to an unirradiated control. The NT structures remain crystalline through irradiation, although TEM reveals the irradiation-induced formation of disordered defect regions in the NTs; these defects are larger in the 250 °C specimen than in the 25 °C specimen. Diffusion of irradiation-induced point defects occurs more readily at 250 °C than at 25 °C, which can explain the resultant agglomeration of larger defect regions in the higher temperature irradiation. These defects subsequently enable enhanced lithium intercalation into the material, explaining the improvement in electrochemical performance observed in the irradiated specimens.

While the unirradiated nanotubes exhibit a reversible capacity of 3.57×10^{-2} mAh cm⁻² at C/12, the TiO₂ electrode irradiated at 25 °C has reversible capacity of 5.39×10^{-2} mAh cm⁻² and the electrode irradiated at 250 °C has a reversible capacity of 6.69×10^{-2} mAh cm⁻². This corresponds to a 33% and 46% increase in capacity for the 25 °C and 250 °C irradiations. It was found by comparing the charge/discharge profiles that an increase in the sloping region, resulting from an increase in defects, contributes to the increase in capacity of the irradiated samples. To better understand the electrochemical behavior, EIS measurements were conducted to calculate lithium diffusivity, which

increased in both irradiated samples. Specifically, unirradiated nanotube electrode shows a Li⁺ diffusivity of $2.3 \times 10^{-13} \, \text{cm}^2 \, \text{s}^{-1}$ compared to $1.0 \times 10^{-12} \, \text{cm}^2$ s^{-1} for the 25 °C irradiated sample and 1.3 \times 10⁻¹¹ cm² s⁻¹ for the 250 °C irradiated sample. Furthermore, electrical conductivity measurements show that for both RT and HT irradiated nanotube samples, the electrical conductivity increased, with the room-temperature irradiation being the highest. These improvements are reflected in the rate capability measurements, in which both irradiated samples outperform the unirradiated control. Interestingly, the high-temperature irradiated sample has the best performance even when cycled at 100 °C, which shows that while electrical conductivity plays an important role, it must be balanced by improvements in ionic conductivity. This study presents a unique perspective on pathways to engineer functional electrode materials by tailoring irradiation conditions.

Acknowledgements

The authors acknowledge support by the National Science Foundation under Grant Nos. DMR-1408949, DMR-1838604, and DMR-1838605. This work was performed, in part, at the Center for Integrated Nanotechnologies, an Office of Science User Facility operated for the U.S. The authors thank A. E. Weltner and P. J. Simmonds for the assistance with the electrical conductivity measurements. Department of Energy (DOE) Office of Science by Los Alamos National Laboratory (Contract DE-AC52-06NA25396) and Sandia National Laboratories (Contract DE-AC04-94AL85000). Use of the Center for Nanoscale Materials, an Office of Science user facility, was supported by the U.S. Department of Energy, Office of Science, Office of Basic Energy Sciences, under Contract No. DE-AC02-06CH11357.

Author contributions

HX designed all experiments. JW and DB designed the ion irradiation experiments. KS and AS prepared the electrodes and conducted electrochemical measurements. KS and DT conducted Raman characterization. YW and DC conducted the proton irradiation experiments. KM and YL conducted TEM and SAED. CD conducted SAED analysis. PB carried out some



electrochemical measurements. KS, HX, and JW analyzed the data. All authors discussed the results and contributed to the manuscript preparation. KS, HX, and JW wrote the manuscript.

Electronic supplementary material: The online version of this article (https://doi.org/10.1007/s108 53-019-03825-w) contains supplementary material, which is available to authorized users.

References

- Bruce PG, Scrosati B, Tarascon JM (2008) Nanomaterials for rechargeable lithium batteries. Angew Chem Int Ed 47:2930–2946
- [2] Deng D, Kim MG, Lee JY, Cho J (2009) Green energy storage materials: nanostructured TiO₂ and Sn-based anodes for lithium-ion batteries. Energy Environ Sci 2:818–837
- [3] Yang ZG, Choi D, Kerisit S et al (2009) Nanostructures and lithium electrochemical reactivity of lithium titanites and titanium oxides: a review. J Power Sources 192:588–598
- [4] Zhu GN, Wang YG, Xia YY (2012) Ti-based compounds as anode materials for Li-ion batteries. Energy Environ Sci 5:6652–6667
- [5] Howard CJ, Sabine TM, Dickson F (1991) Structural and thermal parameters for rutile and anatase. Acta Crystallogr Sect B Struct Sci 47:462–468
- [6] Zachauchristiansen B, West K, Jacobsen T, Atlung S (1988) Lithium insertion in different TiO₂ modifications. Solid State Ionics 28:1176–1182
- [7] Arico AS, Bruce P, Scrosati B, Tarascon JM, Van Schalkwijk W (2005) Nanostructured materials for advanced energy conversion and storage devices. Nat Mater 4:366–377
- [8] Chen JS, Tan YL, Li CM et al (2010) Constructing hierarchical spheres from large ultrathin anatase TiO₂ nanosheets with nearly 100% exposed (001) facets for fast reversible lithium storage. J Am Chem Soc 132:6124–6130
- [9] Kavan L, Kalbac M, Zukalova M et al (2004) Lithium storage in nanostructured TiO₂ made by hydrothermal growth. Chem Mater 16:477–485
- [10] Maier J (2007) Size effects on mass transport and storage in lithium batteries. J Power Sources 174:569–574
- [11] Manthiram A, Murugan AV, Sarkar A, Muraliganth T (2008) Nanostructured electrode materials for electrochemical energy storage and conversion. Energy Environ Sci 1:621–638
- [12] Wagemaker M, Borghols WJH, Mulder FM (2007) Large impact of particle size on insertion reactions. A case for anatase LixTiO₂. J Am Chem Soc 129:4323–4327

- [13] Wang Y, Cao GZ (2008) Developments in nanostructured cathode materials for high-performance lithium-ion batteries. Adv Mater 20:2251–2269
- [14] Yuan Y, Chen F, Cai G et al (2019) Ultrafine TiO₂ nanocrystalline anchored on nitrogen-doped amorphous mesoporous hollow carbon nanospheres as advanced anode for lithium ion batteries. Electrochim Acta 296:669–675
- [15] Li J, Li Y, Lan Q, Yang Z, Lv X-J (2019) Multiple phase N-doped TiO₂ nanotubes/TiN/graphene nanocomposites for high rate lithium ion batteries at low temperature. J Power Sources 423:166–173
- [16] Ma Y, Li Y, Li D, Liu Y, Zhang J (2019) Uniformly distributed TiO₂ nanorods on reduced graphene oxide composites as anode material for high rate lithium ion batteries. J Alloys Compd 771:885–891
- [17] Tarascon JM, Armand M (2001) Issues and challenges facing rechargeable lithium batteries. Nature 414:359–367
- [18] Ortiz GF, Hanzu I, Djenizian T, Lavela P, Tirado JL, Knauth P (2009) Alternative Li-ion battery electrode based on selforganized titania nanotubes. Chem Mater 21:63–67
- [19] Smith KA, Savva AI, Deng C et al (2017) Effects of proton irradiation on structural and electrochemical charge storage properties of TiO₂ nanotube electrodes for lithium-ion batteries. J Mater Chem A 5:11815–11824
- [20] Xiong H, Yildirim H, Podsiadlo P et al (2013) Compositional tuning of structural stability of lithiated cubic titania via a vacancy-filling mechanism under high pressure. Phys Rev Lett 110:078304
- [21] Hahn BP, Long JW, Rolison DR (2013) Something from nothing: enhancing electrochemical charge storage with cation vacancies. Acc Chem Res 46:1181–1191
- [22] Koo B, Chattopadhyay S, Shibata T et al (2013) Intercalation of sodium ions into hollow iron oxide nanoparticles. Chem Mater 25:245–252
- [23] Koo B, Xiong H, Slater MD et al (2012) Hollow iron oxide nanoparticles for application in lithium ion batteries. Nano Lett 12:2429–2435
- [24] Savva AI, Smith KA, Lawson M et al (2018) Defect generation in TiO₂ nanotube anodes via heat treatment in various atmospheres for lithium-ion batteries. Phys Chem Chem Phys 20:22537–22546
- [25] Devanathan R (2009) Radiation damage evolution in ceramics. Nucl Instrum Methods Phys Res Sect B Beam Interact Mater Atoms 267:3017–3021
- [26] Kinoshita C (1991) Characteristics of microstructural evolution of radiation-damage in ceramics under fusion environment. J Nucl Mater 179:53–59
- [27] Zinkle SJ, Kinoshita C (1997) Defect production in ceramics. J Nucl Mater 251:200–217



- [28] Leteurtre J, Soullard J (1973) Irradiation effects in amorphous ZrO₂. Irradiat Eff 20:175–180
- [29] Meldrum A, Boatner LA, Ewing RC (1997) Electron-irradiation-induced nucleation and growth in amorphous LaPO₄, ScPO₄, and zircon. J Mater Res 12:1816–1827
- [30] Yu N, Nastasi M (1995) Ion beam induced epitaxial recrystallization of alumina thin films deposited on sapphire. Nucl Instrum Methods Phys Res Sect B Beam Interact Mater Atoms 106:579–582
- [31] Naguib HM, Kelly R (1970) The crystallization of amorphous ZrO₂ by thermal heating and by ion bombardment. J Nucl Mater 35:293–305
- [32] Zhang L, Jiang W, Ai W, Chen L, Wang T (2018) Ion irradiation induced nucleation and growth of nanoparticles in amorphous silicon carbide at elevated temperatures. J Nucl Mater 505:249–254
- [33] Zhou J, Yao T, Cao D, Lian J, Lu F (2018) In-situ TEM study of radiation-induced amorphization and recrystallization of hydroxyapatite. J Nucl Mater 512:307–313
- [34] Jencic I, Bench MW, Robertson IM, Kirk MA (1995) Electron-beam-induced crystallization of isolated amorphous regions in Si, Ge, GaP, and GaAs. J Appl Phys 78:974–982
- [35] Hollar EP, Robertson IM, Jenčič I (2000) Crystallization of isolated amorphous zones in semiconductor materials. MRS Online Proc Libr 647:R9.4.1/O14.4.1–R9.4.6/O14.4.6
- [36] Toulemonde M, Dufour C, Paumier E (1992) Transient thermal process after a high-energy heavy-ion irradiation of amorphous metals and semiconductors. Phys Rev B 46:14362–14369
- [37] Toulemonde M, Dufour C, Meftah A, Paumier E (2000) Transient thermal processes in heavy ion irradiation of crystalline inorganic insulators. Nucl Instrum Methods Phys Res Sect B Beam Interact Mater Atoms 166:903–912
- [38] Weber WJ (2000) Models and mechanisms of irradiationinduced amorphization in ceramics. Nucl Instrum Methods Phys Res Sect B Beam Interact Mater Atoms 166:98–106
- [39] Zinkle SJ (1996) Irradiation spectrum and ionization-induced diffusion effects in ceramics. MRS Proc 439:667–678
- [40] Backman M, Djurabekova F, Pakarinen OH et al (2012) Cooperative effect of electronic and nuclear stopping on ion irradiation damage in silica. J Phys D Appl Phys 45(50):505305
- [41] Backman M, Djurabekova F, Pakarinen OH et al (2013) Atomistic simulations of MeV ion irradiation of silica. Nucl Instrum Methods Phys Res Sect B Beam Interact Mater Atoms 303:129–132
- [42] Liu P, Zhang Y, Xue H et al (2016) A coupled effect of nuclear and electronic energy loss on ion irradiation damage in lithium niobate. Acta Mater 105:429–437

- [43] Ridgway MC, Djurabekova F, Nordlund K (2015) Ion-solid interactions at the extremes of electronic energy loss: examples for amorphous semiconductors and embedded nanostructures. Curr Opin Solid State Mater Sci 19:29–38
- [44] Smith KA, Savva AI, Wu YQ et al (2018) Effects of intermediate energy heavy-ion irradiation on the microstructure of rutile TiO₂ single crystal. J Am Ceram Soc 101:4357–4366
- [45] Zhang YW, Sachan R, Pakarinen OH et al (2015) Ionizationinduced annealing of pre-existing defects in silicon carbide. Nat Commun 6:8049
- [46] Zarkadoula E, Xue HZ, Zhang YW, Weber WJ (2016) Synergy of inelastic and elastic energy loss: temperature effects and electronic stopping power dependence. Scr Mater 110:2–5
- [47] Shukur HA, Sato M, Nakamura I, Takano I (2012) Characteristics and photocatalytic properties of thin film prepared by sputter deposition and post-N+ ion implantation. Adv Mater Sci Eng 2012:1–7
- [48] Lumpkin GR, Smith KL, Blackford MG et al (2008) Experimental and atomistic modeling study of ion irradiation damage in thin crystals of the TiO₂ polymorphs. Phys Rev B Condens Matter 77:214201
- [49] Rath H, Dash P, Som T et al (2009) Structural evolution of TiO₂ nanocrystalline thin films by thermal annealing and swift heavy ion irradiation. J Appl Phys 105:074311
- [50] Uberuaga BP, Bai XM (2011) Defects in rutile and anatase polymorphs of TiO₂: kinetics and thermodynamics near grain boundaries. J Phys Condens Matter 23:435004
- [51] Qin MJ, Kuo EY, Whittle KR et al (2013) Density and structural effects in the radiation tolerance of TiO₂ polymorphs. J Phys Condens Matter 25:355402
- [52] Li F, Lu P, Sickafus KE (2002) Effects of Xe-ion irradiation at high temperature on single crystal rutile. J Nucl Mater 306:121–125
- [53] Hartmann T, Wang LM, Weber WJ et al (1998) Ion beam radiation damage effects in rutile (TiO₂). Nucl Instrum Methods Phys Res Sect B 141:398–403
- [54] Liu N, Haublein V, Zhou XM et al (2015) "Black" TiO₂ nanotubes formed by high-energy proton implantation show noble-metal-co-catalyst free photocatalytic H-2-evolution. Nano Lett 15:6815–6820
- [55] Xiong H, Slater MD, Balasubramanian M, Johnson CS, Rajh T (2011) Amorphous TiO₂ nanotube anode for rechargeable sodium ion batteries. J Phys Chem Lett 2:2560–2565
- [56] Xiong H, Yildirim H, Shevchenko EV et al (2012) Selfimproving anode for lithium-ion batteries based on amorphous to cubic phase transition in TiO₂ nanotubes. J Phys Chem C 116:3181–3187



- [57] Barnes P, Savva A, Dixon K et al (2018) Electropolishing valve metals with a sulfuric acid-methanol electrolyte at low temperature. Surf Coat Technol 347:150–156
- [58] McCreery RL (2000) Raman Spectroscopy for Chemical Analysis. John Wiley & Sons, New York
- [59] Balachandran U, Eror NG (1982) Raman spectra of titanium dioxide. J Solid State Chem 42:276–282
- [60] Frank O, Zukalova M, Laskova B, Kürti J, Koltai J, Kavan L (2012) Raman spectra of titanium dioxide (anatase, rutile) with identified oxygen isotopes (16, 17, 18). Phys Chem Chem Phys 14:14567–14572
- [61] Porto SPS, Fleury PA, Damen TC (1967) Raman spectra of TiO₂, MgF₂, ZnF₂, FeF₂, and MnF₂. Phys Rev 154:522–526
- [62] Zhang Y, Harris CX, Wallenmeyer P, Murowchick J, Chen X (2013) Asymmetric lattice vibrational characteristics of rutile TiO₂ as revealed by laser power dependent raman spectroscopy. J Phys Chem C 117:24015–24022
- [63] Ohsaka T, Izumi F, Fujiki Y (1978) Raman-spectrum of anatase, TiO₂. J Raman Spectrosc 7:321–324
- [64] Sahoo S, Arora AK, Sridharan V (2009) Raman line shapes of optical phonons of different symmetries in anatase TiO₂ nanocrystals. J Phys Chem C 113:16927–16933
- [65] Scherrer P (1918) Bestimmung der Größe und der inneren Struktur von Kolloidteilchen mittels Röntgenstrahlen. Nachr. Ges. Wiss. Goettingen, Math.-Phys. Kl. 36:98–100
- [66] Bae I-T, Zhang Y, Weber WJ, Higuchi M, Giannuzzi LA (2007) Electron-beam induced recrystallization in amorphous apatite. Appl Phys Lett 90:021912
- [67] Lu F, Shen Y, Sun X, Dong Z, Ewing RC, Lian J (2013) Size dependence of radiation-induced amorphization and recrystallization of synthetic nanostructured CePO₄ monazite. Acta Mater 61:2984–2992
- [68] Yu N, Sickafus KE, Nastasi M (1996) Electron irradiation induced crystallization of amorphous MgAl₂O₄. Mater Chem Phys 46:161–165
- [69] Yang X, Wang R, Yan H, Zhang Z (1997) Low energy electron-beam-induced recrystallization of continuous GaAs amorphous foils. Mater Sci Eng B 49:5–13
- [70] Sina Y, Ishimaru M, McHargue CJ, Alves E, Sickafus KE (2014) Ion beam induced epitaxial crystallization of α-Al₂O₃ at room temperature. Nucl Instrum Methods Phys Res Sect B Beam Interact Mater Atoms 321:8–13
- [71] Behera AK, Facsko S, Bandyopadyay MK, Das S, Chatterjee S (2014) Amorphization and recrystallization of singlecrystalline hydrogen titanate nanowires by N+ ion irradiation. J Appl Phys 115:233505
- [72] Zhang JM, Lian J, Namavar F, Ewing RC (2009) Radiation response of nanocrystalline rutile (TiO₂). Microsc Microanal 15:1366–1367

- [73] Zhang JM, Lian J, Namavar F et al (2011) Nanosized rutile (TiO₂) thin film upon ion irradiation and thermal annealing. J Phys Chem C 115:22755–22760
- [74] Andrés J, Longo E, Gouveia AF, Gracia L, Oliveira MC (2018) In situ formation of metal nanoparticles through electron beam irradiation: modeling real materials from firstprinciples calculations. J Mater Sci Eng 7(3):1000461
- [75] Zhang X, Fu EG, Li N et al (2012) Design of radiation tolerant nanostructured metallic multilayers. J Eng Mater Trans ASME 134:041010
- [76] Zhuo MJ, Fu EG, Yan L et al (2011) Interface-enhanced defect absorption between epitaxial anatase TiO₂ film and single crystal SrTiO₃. Scr Mater 65:807–810
- [77] Uberuaga BP, Smith R, Cleave AR et al (2005) Exploring long-time response to radiation damage in MgO. Nucl Instrum Methods Phys Res Sect B Beam Interact Mater Atoms 228:260–273
- [78] Li FX, Lu P, Sickafus KE (2002) Effects of Xe-ion irradiation at high temperature on single crystal rutile. J Nucl Mater 306:121–125
- [79] Nordlund K, Sundholm D, Pyykko P, Zambrano DM, Djurabekova F (2017) Nuclear stopping power of antiprotons. Phys Rev A 96:042717
- [80] Agnello M, Belli G, Bendiscioli G et al (1995) Antiproton slowing-down in H-2 and He and evidence of nuclear stopping power. Phys Rev Lett 74:371–374
- [81] Smith K, Parrish R, Wei W et al (2016) Disordered 3D multilayer graphene anode material from CO₂ for sodium-ion batteries. Chemsuschem 9:1397–1402
- [82] Orazem ME, Tribollet B (2008) Electrochemical impedance spectroscopy. Wiley, Hoboken
- [83] Levi MD, Salitra G, Markovsky B et al (1999) Solid-state electrochemical kinetics of Li-ion intercalation into Li_{1-x-} CoO₂: simultaneous application of electroanalytical techniques SSCV, PITT, and EIS. J Electrochem Soc 146:1279–1289
- [84] Ruffo R, Hong SS, Chan CK, Huggins RA, Cui Y (2009) Impedance analysis of silicon nanowire lithium ion battery anodes. J Phys Chem C 113:11390–11398
- [85] He BL, Dong B, Li HL (2007) Preparation and electrochemical properties of Ag-modified TiO₂ nanotube anode material for lithium-ion battery. Electrochem Commun 9:425–430
- [86] Ho C, Raistrick ID, Huggins RA (1980) Application of A-C techniques to the study of lithium diffusion in tungsten trioxide thin films. J Electrochem Soc 127:343–350
- [87] Takami N, Satoh A, Hara M, Ohsaki I (1995) Structural and kinetic characterization of lithium intercalation into carbon anodes for secondary lithium batteries. J Electrochem Soc 142:371–379



- [88] Liao AZ, Wang CW, Chen JB, Zhang XQ, Li Y, Wang J (2015) Remarkably improved field emission of TiO₂ nanotube arrays by annealing atmosphere engineering. Mater Res Bull 70:988–994
- [89] Tighineanu A, Ruff T, Albu S, Hahn R, Schmuki P (2010) Conductivity of TiO₂ nanotubes: influence of annealing time and temperature. Chem Phys Lett 494:260–263
- [90] Park M, Zhang XC, Chung MD, Less GB, Sastry AM (2010) A review of conduction phenomena in Li-ion batteries. J Power Sources 195:7904–7929
- [91] Was GS (2007) Fundamentals of radiation materials science: metals and alloys. Springer, Berlin

- [92] Certain A, Kuchibhatla S, Shutthanandan V, Hoelzer DT, Allen TR (2013) Radiation stability of nanoclusters in nanostructured oxide dispersion strengthened (ODS) steels. J Nucl Mater 434:311–321
- [93] Snead LL, Zinkle SJ, White DP (2005) Thermal conductivity degradation of ceramic materials due to low temperature, low dose neutron irradiation. J Nucl Mater 340:187–202

Publisher's Note Springer Nature remains neutral with regard to jurisdictional claims in published maps and institutional affiliations.

